

Kink Dynamics in a Parametric ϕ^6 System: A Model With Controllably Many Internal Modes

A. Demirkaya,^{a,1} R. Decker,^a P. G. Kevrekidis^b I. C. Christov^{c,d} A. Saxena^c

^a*Mathematics Department, University of Hartford,
200 Bloomfield Ave, West Hartford, CT 06117, USA*

^b*Department of Mathematics and Statistics, University of Massachusetts,
Amherst, MA 01003-4515, USA*

^c*Center for Nonlinear Studies and Theoretical Division, Los Alamos National Laboratory,
Los Alamos, NM 87545, USA*

^d*School of Mechanical Engineering, Purdue University,
West Lafayette, IN 47907, USA*

E-mail: demirkaya@hartford.edu, rdecker@hartford.edu,
kevrekid@math.umass.edu, christov@purdue.edu, avadh@lanl.gov

ABSTRACT: We explore a variant of the ϕ^6 model originally proposed in Phys. Rev. D **12**, 1606 (1975) as a prototypical, so-called, “bag” model in which domain walls play the role of quarks within hadrons. We examine the steady state of the model, namely an apparent bound state of two kink structures. We explore its linearization, and we find that, as a function of a parameter controlling the curvature of the potential, an *effectively arbitrary* number of internal modes may arise in the point spectrum of the linearization about the domain wall profile. We explore some of the key characteristics of kink-antikink collisions, such as the critical velocity and the multi-bounce windows, and how they depend on the principal parameter of the model. We find that the critical velocity exhibits a non-monotonic dependence on the parameter controlling the curvature of the potential. For the multi-bounce windows, we find that their range and complexity decrease as the relevant parameter decreases (and as the number of internal modes in the model increases). We use a modified collective coordinates method [in the spirit of recent works such as Phys. Rev. D **94**, 085008 (2016)] in order to capture the relevant phenomenology in a semi-analytical manner.

¹Corresponding author.

Contents

1	Introduction	1
2	Model Setup	3
3	Numerical Results	6
4	Collective Coordinate Approach and Connection to the Numerical Results	11
5	Conclusions and Future Challenges	16
A	Derivation of the Collective Coordinates Effective Lagrangians	17

1 Introduction

The study of field theories of the nonlinear Klein–Gordon type and especially of the general class of ϕ^4 models is a topic of wide appeal and time-honored history [1]. Such models are of interest to a broad array of applications. These range from describing domain walls in cosmology [2, 3] to structural phase transitions [4, 5], uniaxial ferroelectrics or even simple polymeric chains [6, Ch. 9]; see also Refs. [7, 8] and those therein. Note that the usual ϕ^6 model is invoked in the description of first-order transitions [4] in ferroelectric [9], ferroelastic and magnetoelastic [10] crystals, the nematic-to-isotropic transition in liquid crystals [11], the electroweak transition in the early Universe [12] and related field theoretic contexts [13]. A particularly appealing feature that was discovered early on was the existence of a fractal structure [2] in the collisions between the fundamental nonlinear wave structures (a kink and an antikink) in such models. This is a topic that was initiated by the numerical investigations in [8, 14] (see also [1]), and it is still under active investigation both in the physics community (see, e.g., Refs. [15–17] and those therein) and the mathematics community (see, e.g., the mathematical analysis of the relevant mechanism provided in [18]).

On the physics side, there has been a very extensive array of recent studies of different classes of phenomena that challenge many of the traditional perspectives of this problem. The more standard view has been that the internal mode of the ϕ^4 kink and its resonant dynamics with other (e.g., translational and extended) degrees of freedom are responsible for the observation of the multi-bounce windows [2, 8, 14]. However, in recent studies all sorts of “anomalies” have arisen. For instance, models of the ϕ^6 type have been shown to feature multi-bounce windows in the absence of internal modes [19]. Parametric deformations of the ϕ^4 model that introduce additional internal modes have been claimed to

suppress two-bounce windows (in which the kinks do not separate upon colliding once, but twice) [16]. Another perhaps even more troubling feature has stemmed from the work presented in Refs. [20, 21]. These claim that if all terms are included in the collective coordinate models aiming at an effective description of these collisions and originating from (for example) the work of Sugiyama [22] (see also [2]), then significant problems (both practically regarding the computation and, more importantly, regarding the results and conclusion drawn thereof) emerge when attempting a quantitative comparison with direct numerical simulations of the governing partial differential equation (PDE). In addition to all these studies, the broadening phenomenology of kink interactions has also enhanced the interest in studying models of the ϕ^6 , ϕ^8 , ϕ^{10} and even ϕ^{12} types [15, 23–25]. A well-rounded, recent summary encompassing a large volume of works on this theme can be found in [17]. As an aside, it is worthwhile to note in passing that fluctuations (considered also below) in the case of the ϕ^6 model have been recently examined not only at the classical level but also at the quantum level. For instance, the works of [26] and [27] proposed two different procedures for evaluating the quantum corrections to the kink mass.

The aim of the present work is to examine a different type of ϕ^6 model than, e.g., the one studied in most works on this topic (Refs. [15, 17, 19, 28] and those therein). On the one hand, the model we consider is a variant of the usual ϕ^6 model that is potentially of intrinsic interest in its own right within high-energy physics, as it was originally proposed by Christ and Lee [29], where it was presented as a prototypical, so-called, “bag” model in which domain walls play the role of quarks within hadrons. Christ and Lee [29] quantized the one-dimensional scalar field theory whose classical solutions include soliton pairs. This variant has a significant “advantage” over more “rigid” (non-parametric) forms of the model employed in the works of [15, 17, 19, 28], in that it possesses a tunable parameter ϵ , and a topological solitary wave (kink) exists for *all* values of this parameter. Even more importantly for our purposes, as we will see below, the solitary wave contains a *controllable number* of internal modes as the parameter ϵ is varied, and this number progressively grows as $\epsilon \rightarrow 0$. In that light, the ϕ^6 variant from [29] is an excellent platform for exploring the role of internal modes in kink-antikink collision dynamics, the variation of the critical velocity, the formation of multi-bounce windows and all the related notions. Thus, it is exactly this effort that we undertake in this work.

This paper is organized as follows. In section 2, we discuss the general background of the model, following [29] and providing the details of the single kink and its excitation spectrum. Then, in section 3, we explore numerically the collisional dynamics of kinks and antikinks, for different values of the model’s parameter ϵ , as well as the dependence of the critical velocity (for the ultimate separation of the kink and antikink) as a function of the parameter ϵ . In section 4, we connect these purely numerical results to a collective coordinate (CC) description of the phenomenon. In applying the CC theory in its “standard” form, as stemming from the early work of [22], we encountered the same types of problems that have been recently reported in [20, 21]. Therefore, we have opted to make the types of amendments/modifications as in the CC approach proposed in [20, 21]. Most notably, these involve the insertion of a “tuning parameter” q in the CC approach, which we discuss in detail in section 4. We see that, upon suitable tuning of this parameter, the ordinary

differential equations (ODEs), which emulate at a low-dimensional level the ϕ^6 model, produce results that are in close qualitative (and even semi-quantitative) agreement with the full numerical simulation of the governing partial differential equation (PDE). It should be explicitly noted, however, that while the parameter ϵ of the potential will be an intrinsic parameter of the ϕ^6 PDE model considered here, q is a phenomenological parameter inserted at the level of the CC ODE effective description of the system. Hence, q is a different type of parameter, arising during the coarse-graining of the original PDE into a set of ODEs. Finally, in section 5, we summarize our results and present some directions for future research. For completeness, we also include a relevant Appendix, in which we provide the details of the derivation of the complete (“unreduced”) CC theory, from which we have derived the “reduced” CC description of our chosen ϕ^6 model.

2 Model Setup

As discussed above, motivated by the work of Christ and Lee [29], we explore a Klein–Gordon field theory of the ϕ^6 variety (setting $\phi = u$) in the form of the PDE:

$$u_{tt} = u_{xx} - V'(u), \quad (2.1)$$

where the potential is given by

$$V(u) = \frac{1}{8(1 + \epsilon^2)}(u^2 + \epsilon^2)(1 - u^2)^2, \quad (2.2)$$

and it is depicted for several values of ϵ in Fig. 1. Notice that this is not precisely the potential proposed in [29], however for simplicity we have set the parameter μ (controlling the amplitude therein) and the parameter g (controlling the value of the uniform steady state) both to unity, for simplicity. The key parameter remaining in the model is the parameter ϵ , which is connected to the curvature of the potential and is critical to understanding our spectral and dynamical observations below. The stationary solution of the model in Eq. (2.1) is of the form [29]:

$$u = u_0(x) = \frac{\sinh\left(\frac{x}{2}\right)}{\sqrt{1 + \epsilon^{-2} + \sinh^2\left(\frac{x}{2}\right)}}. \quad (2.3)$$

The remarkable feature of this solution, and the reason why it was chosen as a candidate for a simplified one-dimensional “bag” model of quarks within hadrons, is that it does *not* exist in the form of an isolated kink. Instead, it takes the form of two kinks “glued” to each other in the form of a bound state, as shown in Fig. 2 for various choices of ϵ . This is indeed reminiscent, at least conceptually, of the setting of quarks whose total number is conserved, but which possess infinite energy in isolation, while certain multi-quark configurations thereof (in the form of bound states) exist and possess finite energy. Topologically similar “glued” kinks were also discussed in [30] in the context of a ϕ^6 model relevant to first-order phase transitions in materials science.

To make the connection with some of the recent works such as those of [17, 19], let us touch upon the limit of $\epsilon \rightarrow 0^+$. Interestingly, in this limit, our solution given in

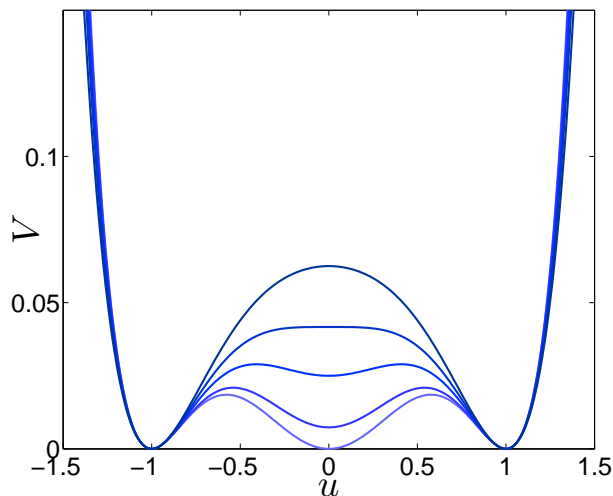


Figure 1. The parametric ϕ^6 potential given in Eq. (2.2) as ϵ is varied from 0.01 to 0.25 to 0.5 to $1/\sqrt{2}$ and to 1 (lighter color curves to darker color curves, respectively), showing the transition from a triple well to a double well. The local minimum at $u = 0$ disappears at $\epsilon = 1/\sqrt{2}$.

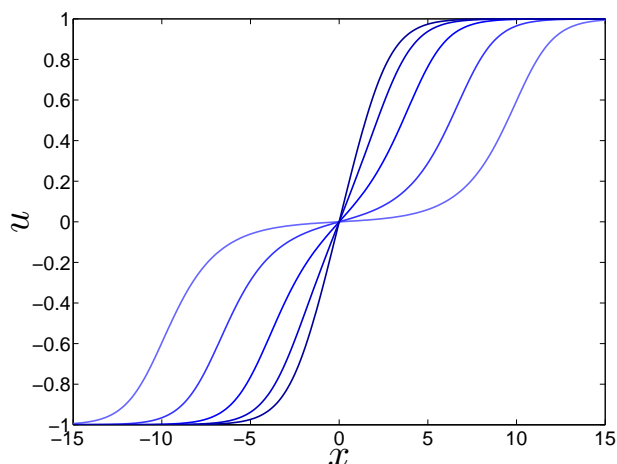


Figure 2. The stationary solution, Eq. (2.3), of our chosen ϕ^6 model, as ϵ is varied from 0.01 to 0.05 to 0.2 to 0.5 and to 1 (lighter color curves to darker color curves, respectively). Clearly, this solution is of the form of two kinks bound together.

Eq. (2.3) degenerates to a vanishing uniform steady state, while the solution explored in the work of [19] is $u \propto \sqrt{(1 + \tanh x)/2}$, connecting the fixed points (“vacuum” states) $u = 0$ and $u = 1$. Furthermore, contrary to what is the case herein, in the $\epsilon \rightarrow 0$ limit there is no internal mode in the linearization spectrum of the steady kink solution. In fact, the latter feature is the important distinguishing trait that the authors of Ref. [19] attribute to their work. In other words, while such internal modes are absent in the kink

linearization spectrum of the kink studied in [19], the collisions between a kink and an antikink *still* feature the resonance windows known, e.g., in the case of the standard ϕ^4 model [8], wherein it was argued that the coupling to the internal mode of the ϕ^4 kink leads to the resonance windows.

On the contrary, a remarkable feature of the model discussed herein, i.e., Eq. (2.1), is that as the curvature-controlling parameter ϵ is decreased, the number of internal modes in the model continues to increase. In particular, an approximate argument in [29] provides support for the number of internal modes being of $O(-\epsilon^{-1} \log \epsilon)$ as $\epsilon \rightarrow 0^+$. In the present work, we will systematically analyze the linearization spectrum of Eq. (2.1) around the bound-state kink solution given in Eq. (2.3). Specifically, we perturb the bound-state solution $u_0(x)$ given in Eq. (2.3) as follows:

$$u(x, t) = u_0(x) + \delta e^{i\omega t} \chi(x), \quad (2.4)$$

then we substitute this ansatz back into Eq. (2.1) and linearize the problem to $O(\delta)$. Next, we solve the resulting linear problem, namely,

$$-\omega^2 \chi = \chi'' - V''(u_0) \chi, \quad (2.5)$$

for the eigenfrequency-eigenvector pair $(\omega, \chi(x))$. In particular, in Fig. 3, the smallest eigenvalues (eigenfrequencies) of the linearization problem are shown. In our current setting of Eq. (2.5) with the potential given in Eq. (2.2), the phonon band (i.e., the continuous spectrum of the problem) extends over the interval $\omega \in (-\infty, -1) \cup (+1, +\infty)$. Hence, eigenfrequencies below $\omega = 1$ in the positive semi-axis of Fig. 3 correspond to internal modes associated with the kink. Of course, in addition to these internal modes, there exists a mode at $\omega = 0$, reflecting the translational invariance of the model. The remaining frequencies ω belonging to the point-spectrum of Eq. (2.5) depend on ϵ .

One natural limit worth considering is that of $\epsilon \rightarrow \infty$. In that case, we revert to the standard, well-known ϕ^4 model situation, which is known to have only one internal mode at $\omega = \sqrt{3}/2$ (in the present units). This is clearly captured accurately in the present numerical computations. We now proceed to explain the picture “shooting down” from that special limit. In so doing, we identify a second internal mode. The latter seems to be asymptotically bifurcating (as $\epsilon \rightarrow \infty$) from the band edge (rather than stemming from a clear-cut, finite value of ϵ). However, additional modes progressively emerge in the point spectrum. These bifurcations can be quantified as occurring at $\epsilon = 0.856$, $\epsilon = 0.356$, $\epsilon = 0.15$, $\epsilon = 0.063$ and $\epsilon = 0.0286$ for the five subsequent ones, giving rise to 7 discernible modes down to the case of $\epsilon = 0.01$ explored here. Furthermore, it should be noted that the dynamics of the first internal mode (the one that exists even as $\epsilon \rightarrow \infty$) appear to be in agreement with the expectation of [29, Fig. 2] (in that work, the additional modes were not systematically probed). An additional observation worth making here concerns the limit of $\epsilon \rightarrow 0^+$. In this limit, as can already be discerned in Fig. 2, the two kinks, constituting the kink of interest herein, “part” from each other, creating two separate kinks one connecting -1 to 0 and one connecting 0 to $+1$. These isolated (in the limit) kinks are “individually” translationally invariant. This rationalizes the approach of a second frequency (pair) to $\omega = 0$ in this limit, reflecting the individual translational invariance of these two kinks.

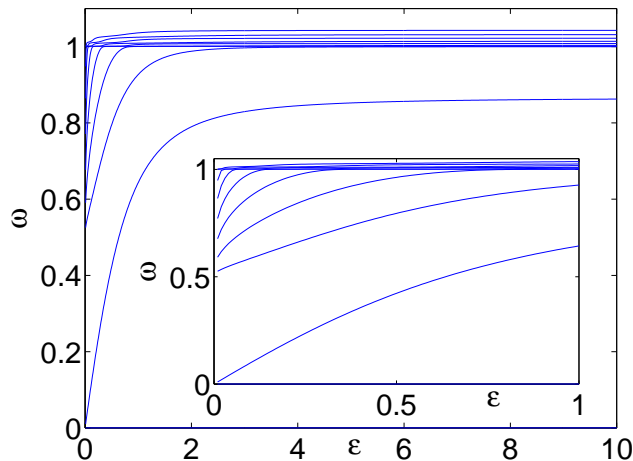


Figure 3. The lowest (positive) eigenfrequencies of the linearization problem given in Eq. (2.5). The phonon band (i.e., the continuous spectrum) starts at $\omega = 1$, hence eigenfrequencies below that critical point are bifurcating internal modes. One can clearly distinguish (also through the inset) the progressive increase in the number of internal modes as $\epsilon \rightarrow 0^+$.

These findings about the internal mode structure and its variation with ϵ lead to some key questions. In particular, it is relevant to identify settings where there is predominantly a single internal mode and compare/contrast them to ones where there are multiple internal modes. For instance, taking $\epsilon = 10$, we have a picture bearing essentially a single internal mode. Then, the collisions between a kink and an antikink should bear the characteristics of two-bounce windows, three-bounce windows and four-bounce windows similar to the intervals obtained in, e.g., [2, Tables I-III]. More modern ways of visualizing the relevant data can be found in, e.g., [19, Fig. 1]. On the other hand, if we lower the value of ϵ , say to $\epsilon = 1$, where visibly two internal modes are present, we would expect kink collision phenomenology to be significantly modified. Subsequent examinations of the cases of, say, $\epsilon = 0.5$ and then $\epsilon = 0.25$ would enable the probing of cases with three and four internal modes. Comparing/contrasting the dynamical outcomes and collisional features of these different cases promises to provide a systematic way to understand the role of internal modes in the kink dynamics. It is, thus, this task that we embark upon next.

3 Numerical Results

In this section we present numerical simulations of the collisions of the kink-antikink pair of Eq. (2.1) for values of $\epsilon \in (0, 20]$. The kink solution is given by $u_0(x)$ in Eq. (2.3), while the antikink is given by $u_0(-x) = -u_0(x)$ for the present case. The initial field configuration is taken to be of the form of a kink (K) plus an antikink (\bar{K}). To consider the collision of moving kinks and antikinks, the stationary solution given in Eq. (2.3) is Lorentz boosted,

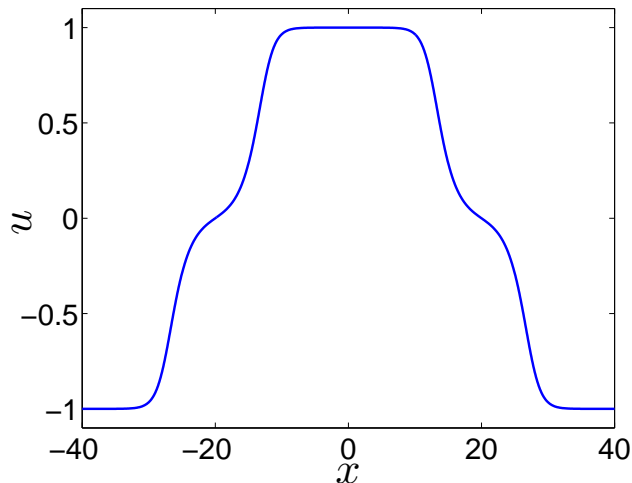


Figure 4. An example of (stationary) kink-antikink configuration with $\epsilon = 0.05$ and $x_0 = 20$.

so that

$$u_K(x, t) = u_0(\gamma(x + x_0 - vt)), \quad u_{\bar{K}}(x, t) = -u_0(\gamma(x - x_0 + vt)),$$

where $\gamma := 1/\sqrt{1-v^2}$, x_0 is where the kink is initially centered such that $2x_0$ is the initial separation between the kink and antikink, and v is the velocity of the moving kink. (The velocity of the moving antikink is $-v$.) Then, the initial conditions for our simulations are given by

$$u(x, 0) = u_K(x, 0) + u_{\bar{K}}(x, 0) - 1, \quad (3.1a)$$

$$u_t(x, 0) = (u_K)_t(x, 0) + (u_{\bar{K}})_t(x, 0), \quad (3.1b)$$

as illustrated in Fig. 4.

To simulate the collisions of kinks and antikinks, we discretized the continuous PDE (2.1) using central finite differences in space, which yields the following semi-discrete set of equations:

$$\ddot{u}_m = \frac{1}{(\Delta x)^2}(u_{m+1} - 2u_m + u_{m-1}) - V'(u_m), \quad (3.2)$$

where over-dots denote time derivatives. For a sufficiently small Δx , typically $\Delta x = 0.1$, the continuous solution is well approximated by $u_m(t) \approx u(x_m, t)$, where $m = 0, 1, 2, \dots, 2N$ and $x_m = (m - N)\Delta x$. The spatial domain is taken to be the interval $[-N\Delta x, N\Delta x]$, where $N = 699$ is used in our simulations. Then, we employ a fourth-order Runge–Kutta method for the evolution in time with a fixed time-step of $\Delta t = 0.001$.

As is well known, the governing PDE (2.1) has Hamiltonian structure, therefore it conserves an energy (Hamiltonian) functional given by

$$H = \mathcal{T}(u; t) + \mathcal{V}(u; t) = \int_{-\infty}^{+\infty} \left(\frac{1}{2}u_t^2 + \frac{1}{2}u_x^2 + V(u) \right) dx, \quad (3.3)$$

where the kinetic \mathcal{T} and potential \mathcal{V} energy contributions of the field, respectively, are

$$\mathcal{T}(u; t) = \frac{1}{2} \int_{-\infty}^{+\infty} u_t^2 dx,$$

$$\mathcal{V}(u; t) = \int_{-\infty}^{+\infty} \left(\frac{1}{2} u_x^2 + V(u) \right) dx.$$

Since $dH/dt = 0$, H is a given constant for a chosen initial field configuration. In our simulations, the average value of H is of $O(1)$, while the deviations from the mean are (for the numerous examples we considered) no more than 10^{-13} . Thus, we have used energy conservation as a check on the validity of our numerical results.

We take the kink and antikink in the initial configuration (3.1) to have equal and opposite initial velocities, $\pm v_{\text{in}}$ (as can always be arranged in this translationally invariant field theory in the center-of-mass frame by a boost transformation of the kink and antikink). The possible outcomes of these collisions are either the so-called multi-bounce scenarios (including as a special case the single bounce one, where the kink and antikink separate immediately after a single collision) or a capture and formation of the so-called bion state [8, 14]. In the former case, an n -bounce represents a scenario for which upon n successive bounces ($n = 1, 2, 3$, etc.) between the kink and antikink, they collect sufficient kinetic energy to escape each other's attraction and finally separate from each other asymptotically. Naturally, for a sufficiently large velocity $v_{\text{in}} > v_c$, for some critical velocity v_c , the canonical scenario is that of $n = 1$. When these waves eventually separate, they escape with equal and opposite velocities $\pm v_{\text{out}}$. On the flip side, when v_{in} tends to zero, it is natural to expect that the kinks do not possess enough kinetic energy to escape each other's attraction. In that case, they will form a very long-lived bound state termed a bion. The multi-bounce windows are interspersed between these two well defined limits (of large and small initial velocity v_{in}).

Following the type of representation given in [18], Fig. 5 shows how the escape velocity v_{out} depends on the initial velocity v_{in} when $\epsilon = 20$, $\epsilon = 1$, $\epsilon = 0.5$ (i.e., going from one internal mode to two and then to three). Note that in order to calculate v_{out} , we performed a linear interpolation of two points (position vs time) and calculated its slope. We made sure that the t values were sufficiently large so that v_{out} remained constant in time. For bigger values of ϵ in Fig. 5(a), as expected, we obtain results similar to [18, 31], since our ϕ^6 model behaves like the classical ϕ^4 model. As ϵ becomes smaller, it gets harder to detect the intervals of n -bounce solutions, see Fig. 5(b,c). It can be observed that as ϵ becomes smaller, i.e., as a larger number of internal modes become available, remarkably the dynamics appears to become “less complex”. In other words, there are fewer multi-bounce windows, and they extend over a narrower band of initial velocities v_{in} . This transition is clear when going from panel (a) to panel (b) in Fig. 5, and perhaps even more dramatically when going from panel (b) to panel (c). This feature appears to be consistent with the corresponding conclusions regarding a parametric double-well model in Ref. [16]. The presence of multiple internal modes decreases the frequencies of the internal vibrations (with ϵ). Apparently, in addition, the presence of multiple internal modes pushes the multi-bounce windows closer to the critical velocity (cf. the analytical predictions for the

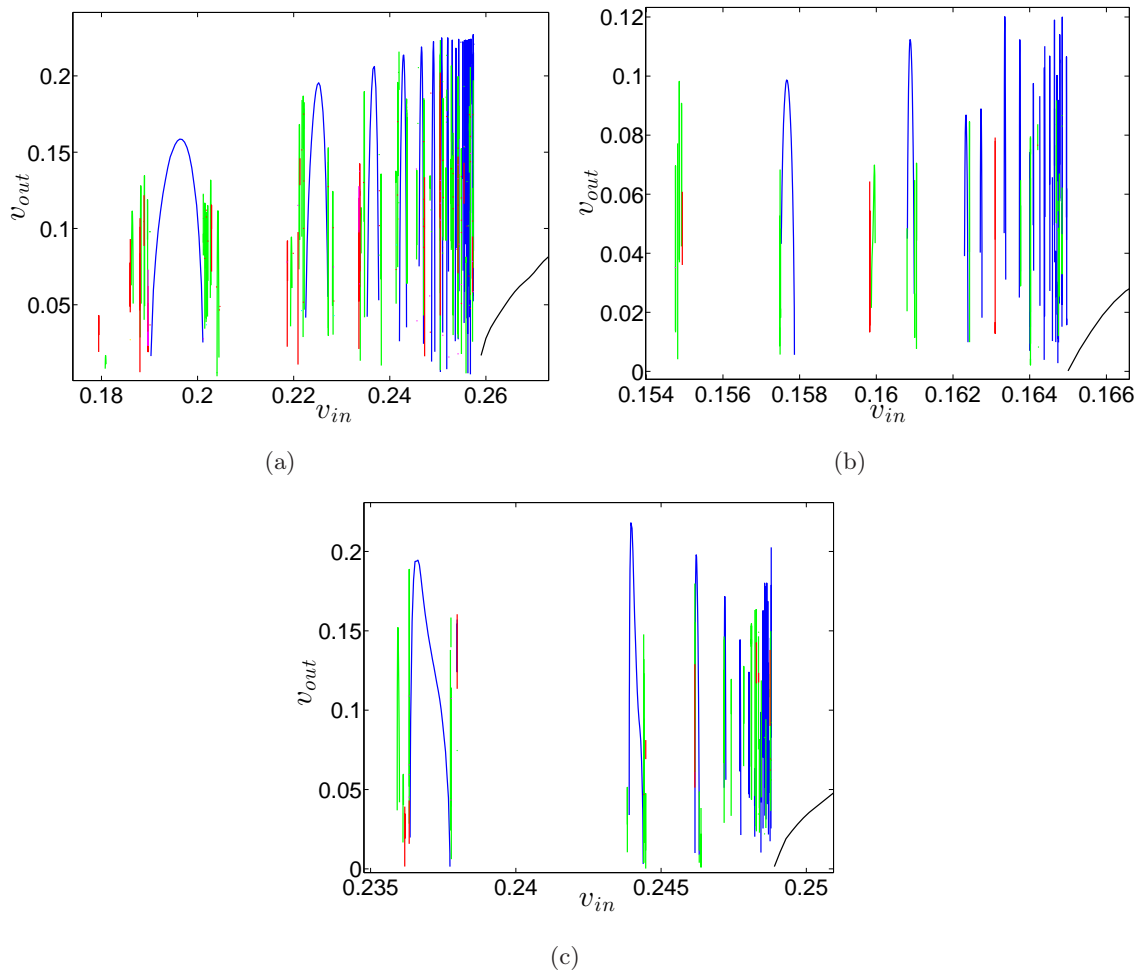


Figure 5. The escape velocity v_{out} as a function of the initial velocity v_{in} when (a) $\epsilon = 20$ (b) $\epsilon = 1$ (c) $\epsilon = 0.5$. Black represents a 1-bounce solution, blue represents a 2-bounce solution, green represents a 3-bounce solution, and red represents a 4-bounce solution.

windows, e.g., in [8, 16]), which also significantly disturbs the delicate resonance structure involved in multi-bounces. The combination of these effects appears to be responsible for the reduction in collisional complexity.

In Fig. 6, we present n -bounce examples in the context of Eq. (2.1) for $n = 1, 2, 3, 4, 5$ and $\epsilon = 1$. In the plots, x_t is the approximate center of the kink (top) and antikink (bottom) as defined by their intersection with the x -axis, and t represents time in the PDE model. Figure 6(c) shows that for an initial velocity $v_{in} = 0.155$, the kink and antikink form a bound pair. This is the bion state discussed above. The other limiting-case scenario is encapsulated in Fig. 6(f), which shows a one-bounce scenario. This occurs when the initial velocity v_{in} is picked greater than the critical velocity v_c , which is the velocity beyond which the kink and antikink with equal and opposite initial velocities collide once, then separate asymptotically. For initial velocities below this critical value, the kink and antikink are

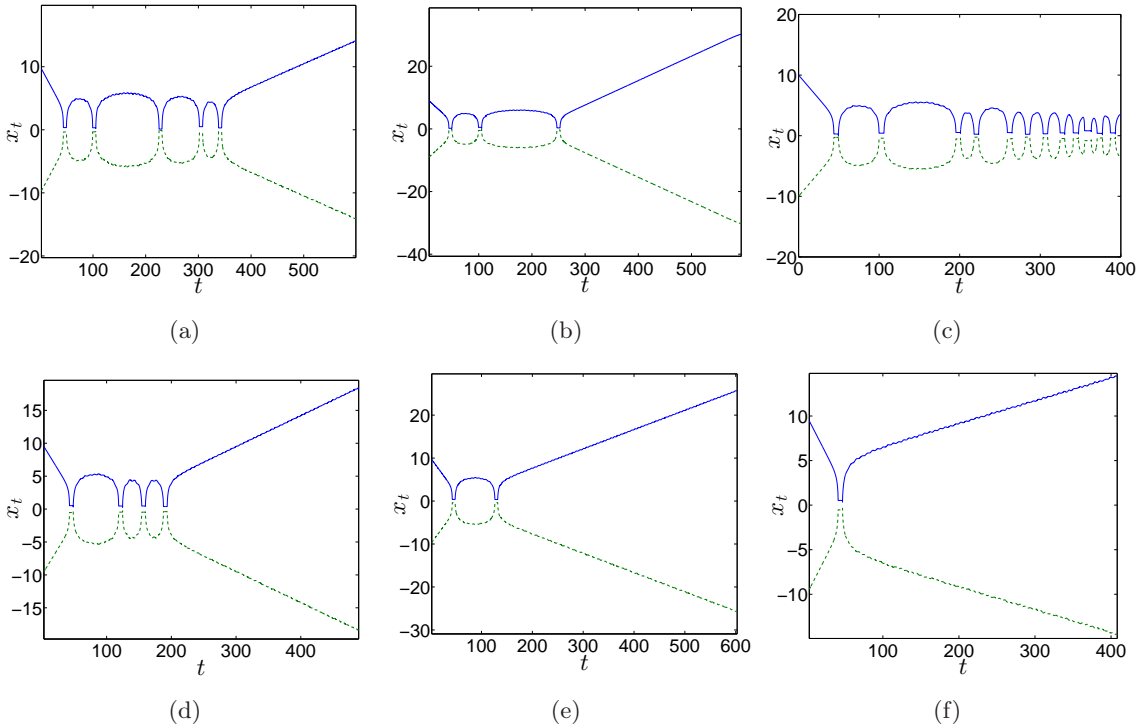


Figure 6. Kink-antikink collisions when $\epsilon = 1$. (a) A 5-bounce solution at $v_{\text{in}} = 0.154761850$. (b) A 3-bounce solution at $v_{\text{in}} = 0.154818$. (c) Capture at $v_{\text{in}} = 0.155$. (d) A 4-bounce solution at $v_{\text{in}} = 0.1598265$. (e) A 2-bounce solution at $v_{\text{in}} = 0.16081$. (f) A 1-bounce solution at $v_{\text{in}} = 0.1665$.

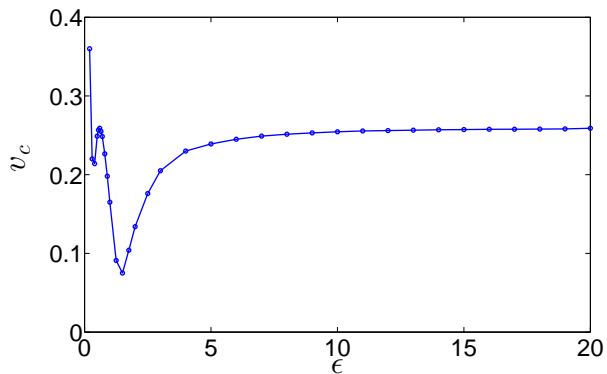


Figure 7. The critical velocity v_c as a function of ϵ . The numerical simulations show that $\epsilon \approx 1.5$ is a cutoff for the monotonic behavior of this function. For any ϵ greater than this cutoff value of 1.5, we see that v_c increases monotonically with ϵ . However, this is not the case for ϵ less than the cutoff value.

either captured or separate eventually after several bounces [see panels (e), (b), (d) and (a) of Fig. 6 for $n = 2, 3, 4$ and 5, respectively].

Importantly, we also show the critical velocity v_c varies with ϵ . Figure 7 shows that

for larger values of ϵ , v_c increases monotonically with ϵ . However, the situation changes for small values of ϵ , and a non-monotonic trend involving oscillations appears to arise as $\epsilon \rightarrow 0^+$. While this may be somewhat surprising in its own right, on the one hand a somewhat similar non-monotonic dependence has been identified as a function of the free parameter in the potential in the work of [16] for a generalized double-well potential. On the other hand, we will see that the CC approach utilized below will be able to capture this phenomenology. It should also be noted that the sextic character of the potential clearly becomes evident for $\epsilon < 1/\sqrt{2}$, when the third well emerges. For $\epsilon > 1/\sqrt{2}$, the potential features a local maximum at the origin (i.e., for $u = 0$), appearing as a double rather than as a triple well potential as illustrated in Fig. 1.

4 Collective Coordinate Approach and Connection to the Numerical Results

In this section, we use the method of collective coordinates (CCs) to understand the kink-antikink interactions studied numerically in the previous section. Following the time-honored tradition of a wide variety of early works, we reduce the PDE (2.1) to a Hamiltonian dynamical system with two degrees of freedom: the kink position $X(t)$ and the magnitude of its internal mode $A(t)$. However, we will follow the prescription of [21], given the problems described therein with regard to utilizing the “standard” CC methodology, which we have encountered as well. In particular, numerical integration of the full ODE system arising in the CC approach breaks down as $X(t) \rightarrow 0$. In order to resolve such problems, as proposed in [21], we assume a colliding kink-antikink system with the following field configuration

$$u(x, t) = u_0(x + X(t)) - u_0(x - X(t)) - \frac{1}{2}[1 + \tanh(qX(t))] + A(t)\left[\chi_\epsilon(x + X(t)) - \chi_\epsilon(x - X(t))\right], \quad (4.1)$$

where $X(t)$, the half the distance between the kink and antikink, and $A(t)$, the amplitude of the internal mode perturbation, are the two degrees of freedom of the CC description. Here, as before, $u_0(x)$ is the stationary kink solution given in Eq. (2.3). In addition, it should be explicitly stated here that our ansatz (4.1) utilizes a collective coordinate based on a linearized (internal) mode of the kink χ_ϵ and its associated lowest (positive) eigenfrequency ω_ϵ of the linearized problem (2.5). Note that the ϵ subscript on $\chi_\epsilon(x)$ and ω_ϵ reminds the reader that they both depend on ϵ and (typically) must be calculated numerically by solving Eq. (2.5). The factor q in Eq. (4.1) was introduced in [21] to avoid some of the pathologies of the standard CC reductions; see the relevant discussion therein. The numerical value of q chosen depends on ϵ , as will be explained below. Finally, we have neglected shape changes of the kinks in the CC ansatz Eq. (4.1) under the assumption that their velocities remain small for most of the duration of their interaction.

Next, we recall that the Lagrangian density for Eq. (2.1) is

$$\mathcal{L} = \frac{1}{2}u_t^2 - \frac{1}{2}u_x^2 - V(u), \quad (4.2)$$

where $V(u)$ is given in Eq. (2.2). Then, the Lagrangian is

$$L = \int_{-\infty}^{+\infty} \mathcal{L} dx = \int \left[\frac{1}{2} u_t^2 - \frac{1}{2} u_x^2 - V(u) \right] dx, \quad (4.3)$$

where henceforth all integrals are understood to be over $x \in (-\infty, +\infty)$. Substituting Eq. (4.1) into Eq. (4.3) yields a lengthy expression. This “unreduced” Lagrangian is given in the Appendix as Eq. (A.2) for completeness. Following [18], we work with a reduced effective Lagrangian that captures the fundamental features:

$$L(X, \dot{X}, A, \dot{A}) = (M_0 + I(X)) \dot{X}^2 - U(X) + \dot{A}^2 - \omega_\epsilon^2 A^2 + 2F(X)A, \quad (4.4)$$

which follows from the general derivation given in the Appendix. Here, overdots denote time derivatives. As shown in the Appendix, F in Eq. (4.4) is given by

$$F(X) = \int [V'(u_0(x+X)) - V'(u_0(x-X))] \chi_\epsilon(x+X) dx \\ - \int V' \left(u_0(x+X) - u_0(x-X) - \frac{1}{2} [1 + \tanh(qX)] \right) \chi_\epsilon(x+X) dx \quad (4.5)$$

and characterizes the interaction between the kink’s translational and internal modes. Meanwhile,

$$M_0 = \int [u'_0(x)]^2 dx \quad (4.6)$$

is the rest mass of the kink, and

$$I(X) = \int u'_0(x+X) u'_0(x-X) dx - \frac{q}{2} \int [u'_0(x+X) + u'_0(x-X)] \operatorname{sech}^2(qX) dx \\ + \frac{q^2}{8} \int \operatorname{sech}^4(qX) dx \quad (4.7)$$

is an effective mass associated with the kink-antikink interaction and the interaction of both the kink and antikink with the field correction proposed by [21]. Here, primes denote differentiation with respect to a function’s argument. Finally,

$$U(X) = \int \frac{1}{2} [u'_0(x+X) - u'_0(x-X)]^2 dx \\ + \int V \left(u_0(x+X) - u_0(x-X) - \frac{1}{2} [1 + \tanh(qX)] \right) dx \quad (4.8)$$

represents an effective potential energy landscape due to the kink-antikink interaction. Typically, $F(X)$, $U(X)$ and $I(X)$ must be evaluated by numerical quadratures. In Fig. 8, we show the functions $F(X)$, $U(X)$ and $I(X)$ for $\epsilon = 0.5, 1$ and 20 . We can see that, while some of these functions roughly maintain the same qualitative characteristics as the parameter ϵ is varied, their quantitative variations are rather significant. We have picked a specific q value for each ϵ . The process of choosing q will be explained below. Our goal is to investigate how the internal mode is excited (i.e., how A evolves) in the kink-antikink collision process.

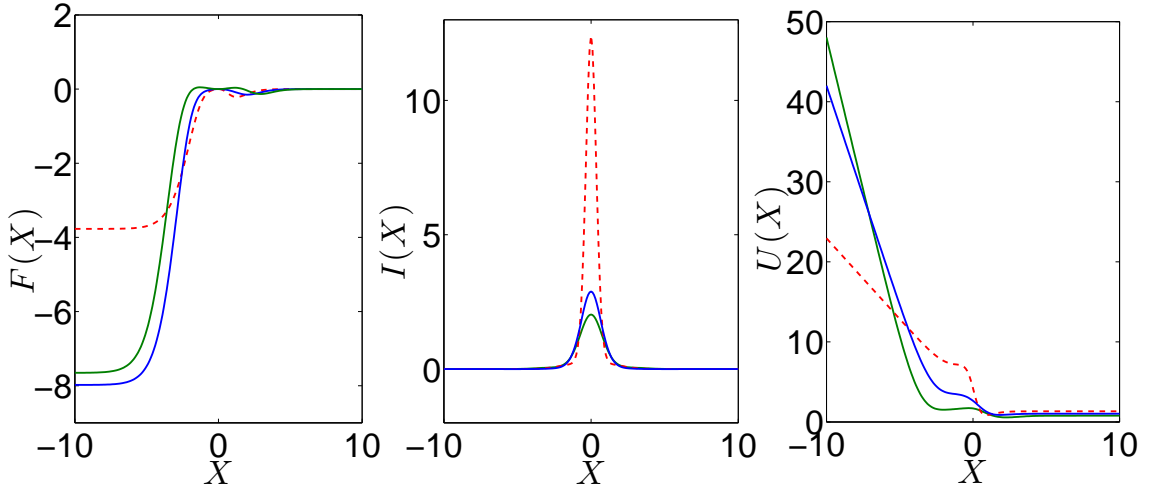


Figure 8. Plots of the functions $F(X)$ (left), $I(X)$ (middle) and $U(X)$ (right) as a function of the position X of the kink’s center, evaluated through the method of collective coordinates, as discussed in the text. Blue corresponds to $\epsilon = 1$, $q = 0.7115$. Green corresponds to $\epsilon = 0.5$, $q = 0.6196$. Dashed red corresponds to $\epsilon = 20$, $q = 1.3917$.

The Euler–Lagrange equations corresponding to Eq. (4.3) are

$$\frac{d}{dt} \left(\frac{\partial L}{\partial \dot{A}} \right) = \frac{\partial L}{\partial A}, \quad (4.9a)$$

$$\frac{d}{dt} \left(\frac{\partial L}{\partial \dot{X}} \right) = \frac{\partial L}{\partial X}. \quad (4.9b)$$

Substituting Eq. (4.4) for L in Eqs. (4.9) yields

$$\ddot{A} = -\omega_\epsilon^2 A + F(X), \quad (4.10a)$$

$$(2M_0 + 2I(X))\ddot{X} = -I'(X)\dot{X}^2 - U'(X) + 2F'(X)A. \quad (4.10b)$$

We solve this second-order system of ODEs, subject to the initial conditions $X(0) = x_0$ and $\dot{X}(0) = v_{\text{in}}$, where x_0 is the initial half-distance between the kink and the antikink, and v_{in} is the initial velocity of the kink. We use MATLAB’s built-in fourth-order Runge–Kutta variable-step size solver `ode45` with built-in error control. We also derive the Euler–Lagrange equations corresponding to the “unreduced” Lagrangian (A.4) and list all the formulæ for the coefficients in the Appendix. The expressions involving integrals which are X -dependent in Eqs. (4.10) are computed by numerical integration.

As mentioned earlier, as $\epsilon \rightarrow \infty$, the ϕ^6 model considered herein converges to the ϕ^4 model. Unfortunately, as discussed in [20, 21], the CC results for the ϕ^4 model presented in [22] contain some misprints. In addition, the reduced system considered therein and in followup works neglects products of and higher-order terms in $A(t)$ and $X(t)$. When the CC formulæ are augmented to include these terms, the results obtained by the ODE system from the CC method do not agree as well with the results of solving the PDE (2.1)

numerically. Specifically, a problem arises when X is very close to 0. In order to overcome these difficulties, in [21], a modification of the field configuration that includes the terms involving the parameter q was proposed:

$$u(x, t) = u_0(x + X(t)) - u_0(x - X(t)) - \tanh(qX) + A(t) \left[\chi(x + X(t)) - \chi(x - X(t)) \right]. \quad (4.11)$$

The latter is to be compared to the the “standard” field configuration introduced in [22], which would take the form

$$u(x, t) = u_0(x + X(t)) - u_0(x - X(t)) - 1 + A(t) \left[\chi(x + X(t)) - \chi(x - X(t)) \right], \quad (4.12)$$

where $\chi(x) = \frac{\sqrt{3}}{2} \tanh(\frac{x}{2}) \operatorname{sech}(\frac{x}{2})$.

In [21], two models were studied, one is the ϕ^4 model that is equivalent to our ϕ^6 model in the limit as $\epsilon \rightarrow \infty$, and the second is the ϕ^6 model corresponding to $\epsilon = 0$ in our model. In [21] it was suggested that a different CC field ansatz be used for each model: (4.11) for the ϕ^4 model, and (4.1) for the ϕ^6 model. Our numerical computations for the model considered herein suggest that for small values of ϵ , a better match between the ODE and PDE results is obtained when ansatz (4.1) is used. For larger values of ϵ , ansatz (4.11) gives a better match. In [21], the value of q was chosen such that the escape velocity of the kink and antikink obtained by the CC approach matches with the escape velocity obtained from the numerical simulations of the PDE. However, then the number of collisions does not match in many cases.

Our aim in the present work is to pick q values such that the ODE results match the PDE results to the fullest extent possible in all respects. In order to find the optimal q for each ϵ , we solve the second-order system of ODEs (4.10). The q value that makes the ODE and the PDE results match when $v_{\text{in}} = v_c$ becomes our optimal choice of q . Picking q in this way allows us to better match the number of bounces predicted by the reduced-ODE model and the PDE. This “optimal” q value is presented in Fig. 9 as a function of ϵ , where we observe a mostly monotonic dependence of q on ϵ . The fitted function (obtained from a standard numerical fitting routine for the range of ϵ shown in Fig. 9) is given by

$$q(\epsilon) = \frac{1.356\epsilon^2 - 1.704\epsilon + 3.179}{\epsilon^2 - 1.609\epsilon + 4.742}. \quad (4.13)$$

For instance, for $\epsilon = 0.5$, the critical velocity is $v_c = 0.2489$ (recall Fig. 7). Solving the reduced-ODE system (4.10) numerically, using MATLAB’s `ode45` with the relative tolerance 10^{-5} and absolute tolerance 10^{-5} , we find that the best agreement between the CC approach and the PDE results occurs when $q = 0.6196$.

In Fig. 10, we show how the kink and antikink centers move in time, by using the CC-based reduced-ODE (4.10) (blue, solid), CC-base full-ODE (A.7) (purple) and the PDE (2.1) (red). These results are based on the optimal value of q , which was computed as described above, thus differently from [21]. In the left panel, we additionally show the effects of slightly perturbing the value of q so as to obtain a much better match between

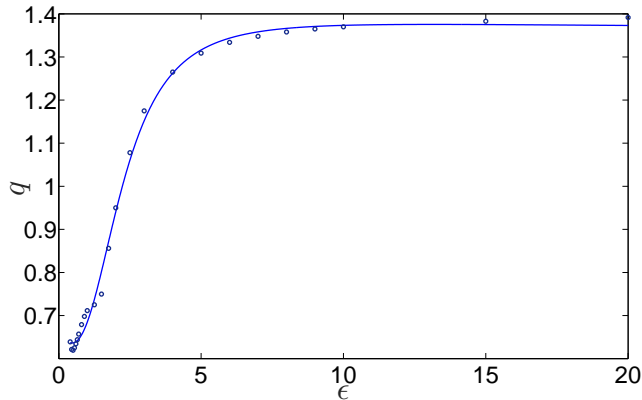


Figure 9. Dependence of the CC ansatz tuning parameter q on the curvature-controlling model parameter ϵ . The data points and the corresponding fitting curve [given in Eq. (4.13)] represent the relation between the “optimal” value of q (under the notion of optimality defined in the text) and our ϕ^6 model’s free parameter ϵ .

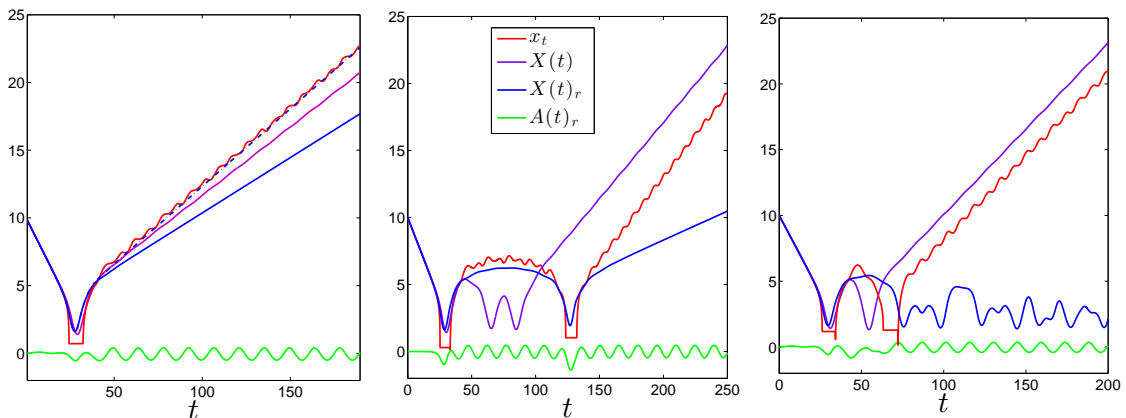


Figure 10. Effect of shape mode(s) and (multi-)bounce windows for $\epsilon = 0.5$, $q = 0.6196$, $v_{\text{in}} = 0.26$ (left), $v_{\text{in}} = 0.24771$ (middle), $v_{\text{in}} = 0.2372$ (right). In each panel, the curves represent the position of kink’s center versus time obtained from: PDE (red), full-ODE (purple), reduced-ODE (blue), and the amplitude of the internal mode for the reduced-ODE (green). The blue dashed curve (left) corresponds to the reduced-ODE model with q perturbing to be 0.6155 in order to obtain a better match.

the reduced-ODE (blue, dashed) and the PDE (red). Each panel in Fig. 10 shows that the results obtained by solving the full-ODE system (A.7) are in some ways better than the ones obtained by solving the reduced-ODE system (4.10). This is the case for most of our simulations. For instance, in the right panel of Fig. 10, we see that reduced-ODE and PDE results do not match at all. However, the number of bounces and escape velocities predicted by the full-ODE system do match the PDE. In the middle panel of Fig. 10, the

reduced-ODE and the PDE results approximately match for a while but then the kink escape velocities disagree between the two approaches. On the other hand, the number of bounces of the full-ODE system and PDE-system do not match but their escape velocities do. Note that the full-ODE system is less sensitive to a change in q .

The results obtained by using the collective coordinates method show that for any $\epsilon \geq 0.3$, there exists a $q > 0$ such that any n -bounce solution that solves the PDE (2.1) can be approximated. In order to obtain a better match, a very small perturbation of q (within the range of ± 0.005) is sufficient; of course, on the flip side, these results suggest the sensitivity of the comparison to the precise value of q . However, the gross features of the collisions for any given ϵ can be obtained by a particular value of q based on the monotonic correspondence given above in Eq. (4.13). The numerical results obtained in Section 3 show the relation between the critical velocity v_c and ϵ as in Fig. 7. The CC method can capture this complex, non-monotonic dependence as shown in Fig. 11. However, when $0 < \epsilon < 0.3$, the CC results are not as accurate as the numerical solutions of the PDE. This feature, however, can be rationalized on the basis of the large number of internal modes that emerge as $\epsilon \rightarrow 0$, whose intricate effects on the dynamics are not captured by the coarse-grained (yet already rather complicated at the level of equations of motion) CC ansatz described above.

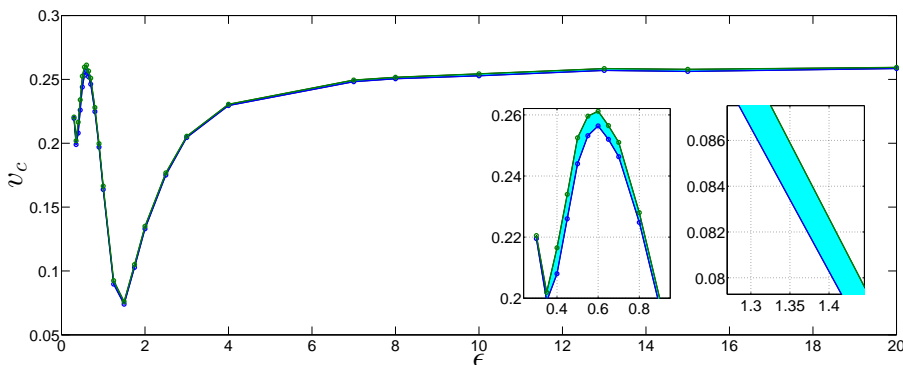


Figure 11. The critical velocity v_c as a function of ϵ found via the method of collective coordinates. The plot shows a region between two curves. The inset plots are magnified views. If q is the optimal value for a given ϵ , then for values in the interval $q \pm 0.005$, v_c should lie in the shaded region.

5 Conclusions and Future Challenges

In the present work, we have revisited an intriguing mono-parametric variant of the ϕ^6 nonlinear field theory. This variant has numerous appealing features, including the existence of an exact analytical solution, a smooth variation of the potential from a triple well (ϕ^6 type) to a double well (ϕ^4 type), the controllable emergence of progressively many internal modes (as the parameter ϵ is reduced, recall Fig. 1), among others. These features led us to reconsider the collisions between a kink and an antikink more generally. Such collisions

were found to possess atypical features such as: (a) progressively narrower and less complex (in their structure) multi-bounce windows and (b) a non-monotonic dependence of the critical velocity of the kink and antikink for a single bounce event as a function of the potential parameter ϵ ; this led us to (c) consider a modified form of the collective coordinates (CCs) approach, based on [21], which enables us to capture qualitatively and even semi-quantitatively the corresponding dynamics using a two-degrees-of-freedom formulation with a tunable parameter $q(\epsilon)$.

Our results are important for scalar field theory models [13] and more broadly for first-order phase transitions [4, 10]. Naturally, these findings pave the way for a number of interesting studies in the future. Motivated by the findings of both the present work and that of [16], it is becoming especially relevant to understand, from a qualitative perspective, the modification of the multi-bounce windows and the non-monotonic dependence of the critical velocity on parameters smoothly deforming the model's potential. Hopefully, the collective coordinates method used here will provide an avenue for further analysis (e.g., in the spirit of [31]) in this direction.

Another question is whether models with more collective coordinates are relevant, and whether it is possible to identify tangible ways in which these additional CCs come into play, as the parameters of the models are varied (and such modes bifurcate). While the methodology developed in [21] appears to work well overall for our problem (one could argue that it can be made/tweaked to work even extremely well), it still perhaps lacks a solid theoretical (conceptual) foundation, at least as far as the choice of the tunable parameter q is concerned. These are important questions that we believe will open new avenues in a problem that was, arguably, long thought to have been definitively addressed. As such, we believe that these questions are certainly worthwhile of further study and relevant results will be accordingly reported in future publications.

A Derivation of the Collective Coordinates Effective Lagrangians

We define $u_{\pm} := \pm u_0(x \pm X(t))$ and $\chi_{\pm} := \pm \chi_{\epsilon}(x \pm X(t))$, hence $u'_{\pm} := \pm u'_0(x \pm X(t))$ and $\chi'_{\pm} := \pm \chi'_1(x \pm X(t))$. Then, Eq. (4.1) becomes

$$u(x, t) = u_+ + u_- - \frac{1}{2}[1 + \tanh(qX)] + A(\chi_+ + \chi_-). \quad (\text{A.1})$$

Substituting Eq. (A.1) into Eq. (4.3) yields

$$L = \int \left\{ \frac{1}{2} \left[\left(u'_+ - u'_- - \frac{q}{2} \operatorname{sech}^2(qX) \right) \dot{X} + \dot{A}(\chi_+ + \chi_-) + A(\chi'_+ - \chi'_-) \dot{X} \right]^2 \right\} dx - \int \left\{ \frac{1}{2} \left[(u'_+ + u'_-) + A(\chi'_+ + \chi'_-) \right]^2 \right\} dx - \int V(u) dx. \quad (\text{A.2})$$

For $V(u)$, we first write $u = u_a + u_b$ where $u_a = u_+ + u_- - \frac{1}{2}[1 + \tanh(qX)]$ and $u_b = A(\chi_+ + \chi_-)$. Then, using a (finite) Taylor series, we get

$$\begin{aligned} V(u) &= V(u_a + u_b) \\ &= V(u_a) + V'(u_a)u_b + \frac{V''(u_a)}{2!}u_b^2 + \frac{V'''(u_a)}{3!}u_b^3 + \frac{V^{(iv)}(u_a)}{4!}u_b^4 \\ &\quad + \frac{V^{(v)}(u_a)}{5!}u_b^5 + \frac{V^{(vi)}(u_a)}{6!}u_b^6. \end{aligned} \quad (\text{A.3})$$

Since V is a sixth degree polynomial, we have no higher terms in the Taylor series expansion. Writing V in this way allows us to keep track of the higher-order terms involving A more easily.

Now, the CC Lagrangian (A.2) takes the ‘‘unreduced’’ form

$$\begin{aligned} L(X, \dot{X}, A, \dot{A}) &= a_0(X) + a_1(X)A + a_2(X)A^2 + a_3(X)\dot{X}^2 + a_4(X)\dot{A}^2 + a_5(X)\dot{A}\dot{X} \\ &\quad + a_6(X)A\dot{A}\dot{X} + a_7(X)A\dot{X}^2 + a_8(X)A^2\dot{X}^2 + a_9(X)A^3 + a_{10}(X)A^4 \\ &\quad + a_{11}(X)A^5 + a_{12}(X)A^6. \end{aligned} \quad (\text{A.4})$$

Writing the effective CC Lagrangian in this way highlights the order of each term though it is simply a formal manipulation to introduce the set of X -dependent coefficients $\{a_i\}_{i=1,2,\dots,12}$. The formulæ of the coefficients in Eq. (A.4) are given below. Note that they are all functions of $X(t)$. Since $\chi_\epsilon(x)$ is not known explicitly for every value of ϵ , the coefficients are presented in integral form. These coefficients are calculated via numerical quadratures. Note that in the derivation of these coefficients, we repeatedly use the fact that a shifted function has the same integral on an infinite interval as the unshifted one. For example, $\int [u_+(x)]^2 dx = \int [u_0(x)]^2 dx = \int [u_-(x)]^2 dx$, all of which are constants.

First,

$$\begin{aligned} a_0(X) &= - \int \frac{1}{2} [u'_0(x+X) - u'_0(x-X)]^2 dx \\ &\quad - \int V \left(u_0(x+X) - u_0(x-X) - \frac{1}{2}[1 + \tanh(qX)] \right) dx, \end{aligned} \quad (\text{A.5})$$

and $U(X) = -a_0(X)$ as given in Eq. (A.5).

Next,

$$a_1(X) = \int - (u'_+ + u'_-) (\chi'_+ + \chi'_-) - V' \left(u_+ + u_- - \frac{1}{2}[1 + \tanh(qX)] \right) (\chi_+ + \chi_-) dx.$$

Applying integration by parts on the first term of the last equation, we get

$$a_1(X) = \int (u''_+ + u''_-) (\chi_+ + \chi_-) - V' \left(u_+ + u_- - \frac{1}{2}[1 + \tanh(qX)] \right) (\chi_+ + \chi_-) dx.$$

Using the fact that u_0 is the steady-state solution of Eq. (2.1), we obtain

$$\begin{aligned} a_1(X) &= \int [V'(u_+) - V'(u_-)] (\chi_+ + \chi_-) \\ &\quad - V' \left(u_+ + u_- - \frac{1}{2}[1 + \tanh(qX)] \right) (\chi_+ + \chi_-) dx. \end{aligned}$$

Finally, by symmetry $X \rightarrow -X$, we get

$$a_1(X) = 2 \int \left\{ [V'(u_+) - V'(u_-)] - V' \left(u_+ + u_- - \frac{1}{2}[1 + \tanh(qX)] \right) \right\} \chi_+ dx.$$

Note that $F(X) = a_1(X)/2$ as given in Eq. (4.5).

Next,

$$a_2(X) = \int -\frac{1}{2} (\chi'_+ + \chi'_-)^2 dx - \int \frac{1}{2} V'' \left(u_+ + u_- - \frac{1}{2}[1 + \tanh(qX)] \right) (\chi_+ + \chi_-)^2 dx. \quad (\text{A.6})$$

Expanding the first integral in Eq. (A.6), then applying integration by parts, and finally using Eq. (2.5) gives

$$\begin{aligned} -\frac{1}{2} \int (\chi'_+ + \chi'_-)^2 dx &= -\int \chi'^2_+ dx - \int \chi'_+ \chi'_- dx \\ &= \int \chi''_+ \chi_+ dx - \int \chi'_+ \chi'_- dx \\ &= \int [-\omega_\epsilon^2 + V''(u_+)] \chi^2_+ dx - \int \chi'_+ \chi'_- dx \\ &= -\omega_\epsilon^2 + \int V''(u_+) \chi^2_+ dx - \int \chi'_+ \chi'_- dx. \end{aligned}$$

Expanding the second integral in Eq. (A.6) gives

$$\begin{aligned} -\int \frac{1}{2} V'' \left(u_+ + u_- - \frac{1}{2}[1 + \tanh(qX)] \right) (\chi_+ + \chi_-)^2 dx \\ = -\int V'' \left(u_+ + u_- - \frac{1}{2}[1 + \tanh(qX)] \right) (\chi^2_+ + \chi_+ \chi_-) dx. \end{aligned}$$

Adding the two integrals and rearranging the terms, Eq. (A.6) becomes

$$\begin{aligned} a_2(X) &= -\omega_\epsilon^2 + \int \left\{ V''(u_+) - V'' \left(u_+ + u_- - \frac{1}{2}[1 + \tanh(qX)] \right) \right\} \chi^2_+ dx \\ &\quad - \int \chi'_+ \chi'_- - V'' \left(u_+ + u_- - \frac{1}{2}[1 + \tanh(qX)] \right) \chi_+ \chi_- dx. \end{aligned}$$

Note that for the reduced system, we only take the first term: $-\omega_\epsilon^2$ as the coefficient of A^2 .

Next,

$$\begin{aligned} a_3(X) &= \int \frac{1}{2} \left[u'_+ - u'_- - \frac{q}{2} \operatorname{sech}^2(qX) \right]^2 dx \\ &= \int [u'_0(x)]^2 dx - \int u'_+ u'_- dx - \frac{q}{2} \int (u'_+ - u'_-) \operatorname{sech}^2(qX) dx \\ &\quad + \frac{q^2}{8} \int \operatorname{sech}^4(qX) dx. \end{aligned}$$

Note that $a_3(X) = M_0 + I(X)$, where M_0 and $I(X)$ are given in Eqs. (4.6) and (4.7), respectively.

Next,

$$a_4(X) = \int \frac{1}{2}(\chi_+ + \chi_-)^2 dx = \int \chi_+^2 dx + \int \chi_+ \chi_- dx = 1 + \int \chi_+ \chi_- dx.$$

Note that for the reduced system, we only take the first term: 1 as the coefficient of \dot{A}^2 .

The remaining coefficients are

$$\begin{aligned} a_5(X) &= \int \left[u'_+ - u'_- - \frac{q}{2} \operatorname{sech}^2(qX) \right] (\chi_+ + \chi_-) dx \\ &= -2 \int u'_- \chi_+ dx - \int \frac{q}{2} \operatorname{sech}^2(qX) (\chi_+ + \chi_-) dx, \\ a_6(X) &= \int (\chi_+ + \chi_-) (\chi'_+ - \chi'_-) dx, \\ a_7(X) &= \int \left[u'_+ - u'_- - \frac{q}{2} \operatorname{sech}^2(qX) \right] (\chi'_+ - \chi'_-) dx, \\ a_8(X) &= \frac{1}{2} \int (\chi'_+ - \chi'_-)^2 dx, \\ a_9(X) &= -\frac{1}{6} \int V''' \left(u_+ + u_- - \frac{1}{2} [1 + \tanh(qX)] \right) (\chi_+ + \chi_-)^3 dx, \\ a_{10}(X) &= -\frac{1}{24} \int V^{(iv)} \left(u_+ + u_- - \frac{1}{2} [1 + \tanh(qX)] \right) (\chi_+ + \chi_-)^4 dx, \\ a_{11}(X) &= -\frac{1}{120} \int V^{(v)} \left(u_+ + u_- - \frac{1}{2} [1 + \tanh(qX)] \right) (\chi_+ + \chi_-)^5 dx, \\ a_{12}(X) &= -\frac{1}{720} \int V^{(vi)} \left(u_+ + u_- - \frac{1}{2} [1 + \tanh(qX)] \right) (\chi_+ + \chi_-)^6 dx. \end{aligned}$$

Finally, the Euler–Lagrange equations (4.9) for the CC Lagrangian (A.4) are

$$\begin{aligned} [a_5(X) + a_6(X)A] \ddot{X} + 2a_4(X) \ddot{A} &= -2a'_4(X) \dot{X} \dot{A} + [a'_7(X) - a'_5(X)] \dot{X}^2 \\ &+ [2a_8(X) - a'_6(X)] A \dot{X}^2 + a_1(X) + 2a_2(X)A \\ &+ 3a_9(X)A^2 + 4a_{10}(X)A^3 + 5a_{11}(X)A^4 + 6a_{12}(X)A^5, \end{aligned} \tag{A.7a}$$

$$\begin{aligned} [2a_3(X) + 2a_7(X)A + 2a_8(X)A^2] \ddot{X} \\ + [a_5(X) + a_6(X)A] \ddot{A} &= -a'_3(X) \dot{X}^2 - a'_7(X) A \dot{X}^2 + [a'_4(X) - a_6(X)] \dot{A}^2 \\ &- 2a_7(X) \dot{A} \dot{X} - a'_8(X) A^2 \dot{X}^2 - 4a_8(X) A \dot{A} \dot{X} \\ &+ a'_0(X) + a'_1(X)A + a'_2(X)A^2 + a'_9(X)A^3 \\ &+ a'_{10}(X)A^4 + a'_{11}(X)A^5 + a'_{12}(X)A^6. \end{aligned} \tag{A.7b}$$

Here, primes denote derivatives with respect to the argument of the function, specifically X . However, for the reasons discussed in [20, 21], we work with the reduced CC Lagrangian (4.4), which corresponds to the system with the coefficients $\{a_i\}_{i=1,2,\dots,5}$ in the main text above.

Acknowledgments

During the initial stages of this work, I.C.C. was partially supported by the LANL/LDRD Program through a Feynman Distinguished Fellowship at Los Alamos National Laboratory (LANL). LANL is operated by Los Alamos National Security, L.L.C. for the National Nuclear Security Administration of the U.S. Department of Energy under Contract No. DE-AC52-06NA25396. P.G.K. gratefully acknowledges support from the Alexander von Humboldt Foundation, the Stavros Niarchos Foundation (via the Greek Diaspora Fellowship Program) and the US National Science Foundation via grant PHY-1602994.

References

- [1] T.I. Belova and A.E. Kudryavtsev, *Phys. Usp.* **40**, 359 (1997).
- [2] P. Anninos, S. Oliveira, and R.A. Matzner, *Phys. Rev. D* **44**, 1147 (1991).
- [3] A. Vilenkin and E.P.S. Shellard, *Cosmic Strings and Other Topological Defects*, Cambridge University Press (Cambridge, 2000).
- [4] Y.M. Gufan, *Structural Phase Transitions* [in Russian], Nauka (Moscow, 1982).
- [5] S.N. Behera and A. Khare, *Pramana (J. of Phys.)* **15**, 245 (1980).
- [6] T. Vachaspati, *Kinks and Domain Walls: An Introduction to Classical and Quantum Solitons*, Cambridge University Press (Cambridge, 2006).
- [7] N. Manton, P. Sutcliffe, *Topological Solitons*, Cambridge University Press (Cambridge, 2004).
- [8] D.K. Campbell, J.F. Schonfeld, and C.A. Wingate, *Physica* **9D**, 1 (1983).
- [9] W.W. Cao and L.E. Cross, *Phys. Rev. B* **44**, 5 (1991).
- [10] A. Planes, E. Obrado, A. Gonzales-Comas, and L. Manosa, *Phys. Rev. Lett.* **79**, 3927 (1997).
- [11] S. Chandrasekhar, *Liquid Crystals* (Cambridge University Press, Cambridge, UK, 1992).
- [12] E.W. Kolb and M.S. Turner, *The Early Universe* (Addison-Wesley, Reading, MA, 1990).
- [13] V.G. Makhankov, *Soliton Phenomenology* (Kluwer Academic, Boston, MA, 1990).
- [14] D.K. Campbell and M. Peyrard, *Physica D* **18**, 47 (1986); *ibid.* **19**, 165 (1986).
- [15] V.A. Gani, A.E. Kudryavtsev, and M.A. Lizunova, *Phys. Rev. D* **89**, 125009 (2014), arXiv:1402.5903.
- [16] F.C. Simas, A.R. Gomes, K.Z. Nobrega, and J.C.R.E. Oliveira, *JHEP* **09**, 104 (2016), arXiv:1605.05344.
- [17] A. Moradi Marjaneh, V.A. Gani, D. Saadatmand, S.V. Dmitriev, and K. Javidan, *JHEP* **07**, 028 (2017), arXiv:1704.08353.
- [18] R.H. Goodman and R. Haberman, *SIAM J. Appl. Dyn. Sys.* **4**, 1195 (2005).
- [19] P. Dorey, K. Mersh, T. Romanczukiewicz, and Y. Shnir, *Phys. Rev. Lett.* **107**, 091602 (2011), arXiv:1101.5951.
- [20] H. Weigel, *J. Phys. Conf. Ser.* **482**, 012045 (2014), arXiv:1309.6607.
- [21] I. Takyi and H. Weigel, *Phys. Rev. D* **94**, 085008 (2016), arXiv:1609.06833.
- [22] T. Sugiyama, *Prog. Theor. Phys.* **61**, 1550 (1979).

- [23] V.A. Gani, V. Lensky, and M.A. Lizunova, JHEP **08** 147 (2015), arXiv:1506.02313.
- [24] A. Khare, I.C. Christov, and A. Saxena, Phys. Rev. E **90**, 023208 (2014), arXiv:1402.6766.
- [25] E. Belendryasova, V.A. Gani, arXiv:1708.00403.
- [26] A. Alonson Izquierdo and J. Mateos Guilarte, Nucl. Phys. B **852**, 696 (2011).
- [27] H. Weigel, Phys. Lett. B **766**, 65 (2017), arXiv:1612.08641.
- [28] M.A. Lohe, Phys. Rev. D **20**, 3120 (1979).
- [29] N.H. Christ and T.D. Lee, Phys. Rev. D **12**, 1606 (1975).
- [30] M. Sanati and A. Saxena, J. Phys. A: Math. Gen. **32**, 4311 (1999).
- [31] R.H. Goodman, A. Rahman, M.J. Bellanich, and C.N. Morrison, Chaos **25**, 043109 (2015), arXiv:1503.08315.